RESEARCH ARTICLE

INTERNATIONAL RESEARCH JOURNAL OF MULTIDISCIPLINARY TECHNOVATION

Asian Research Association

DOI: 10.54392/irjmt25117

Bismuth Vanadate Microspheres: Utilizing Temperature-driven Phase Transition for Improved Sunlight-Driven Photocatalysis and Antibacterial Efficacy

Rehna Parameswaran [a], Senthil Kumar Nagarajan [a,*], Chandrasekar Sivakumar [b], Balachandran Subramanian [c,*], Raju S [d], Mohanraj Kumar [e]

[a] Department of Physics, Nanotechnology Lab, Kongunadu Arts and Science College, Coimbatore-641029, Tamil Nadu, India
[b] Department of Physics, National Chung Hsing University, Taichung - 40227, Taiwan
[c] Functional Materials and Materials Chemistry Laboratory, Department of Physiology, Saveetha Dental College and Hospitals, Saveetha Institute of Medical and Technical Sciences, Saveetha University, Chennai, 600077, Tamil Nadu, India
[d] Department of Physics, KPR Institute Engineering and Technology, Coimbatore, 641 407, Tamilnadu, India
[e] Department of Environmental Engineering and Management, Chaoyang University of Technology, Taichung, 413310, Taiwan
* Corresponding Authors Email: kumarsrkvphy@gmail.com, balachem13@gmail.com

DOI: https://doi.org/10.54392/irjmt25117
Received: 11-08-2024; Revised: 16-01-2025; Accepted: 24-01-2025; Published: 30-01-2025

Abstract: In this work, bismuth vanadate ($BiVO_4$) microspheres are synthesized using a simple, cost effective, co-precipitation technique. This study investigates how the annealing temperature influences the photocatalytic and antimicrobial properties of nanoparticles made of $BiVO_4$. Examining the phase structure, chemical compounds state, composition of chemicals, shape, as well as optical characteristics of the prepared materials, by using X-ray diffraction (XRD), scanning electron microscopy (SEM), Energy dispersive X-ray spectroscopy (EDS), high-resolution transmission electron microscopy (HR-TEM), X-ray photoelectron spectroscopy (XPS), Raman analysis, UV-Vis diffuse reflectance spectroscopy (DRS), Photoluminescence (PL) spectroscopy studies. Based on XRD analysis data, $BiVO_4$ exhibits a phase change of the tetragonal structure to monoclinic at 500 °C ($BiVO_4$@500 °C). It is interesting to note that under sunlight irradiation, $BiVO_4$ nanoparticles annealed at 500 °C show excellent photocatalytic behavior in opposition to the dye methylene blue ($k = 0.0151\ min^{-1}$). According to investigations on the development of antibacterial activity through the utilization of BiVO4@500 °C sample by well diffusion method appears to be an effective growth inhibitor of both gram-positive and gram-negative bacteria, such as *Bacillus subtilis (B. subtilis), Staphylococcus aureus (S. aureus*), *Escherichia coli (E. coli), Proteus vulgaris (P. vulgaris*)), respectively.

Keywords: $BiVO_4$, Pollutant, Pathogens, Water Purification

1. Introduction

Water contamination is causing serious problems for the world's ecosystem and water availability. The increasing worldwide population causes pollution to worsen in several aquatic ecosystems, including soil, air, and water. It has been necessary to mobilize a global effort to mitigate environmental damage. Diverse organic compounds including dyes, hospital drug waste and animal husbandry, and agricultural chemicals, which include fertilizers, fungicides, insecticides, herbicides, and pesticides, are the main environmental pollutants. A significant amount of the contaminants found in wastewater are caused by organic dyes used in the textile and dye industries [1-3]. Untreated effluent from these sectors can cause a range of diseases when it combines with water bodies. Because it contains a variety of organic dyes and bacteria that taint water bodies and seriously harm creatures. Among the dyes employing in the textile industry, those containing a benzidine moiety are notable for their bio-calcitrance. A common phenothiazine derivative used to color cotton, wool, and silk is methylene blue (MB). Methylene blue was very poisonous and carcinogenic, rendering them hazardous to humans and animals. The treatment of wastewater containing such pigments is essential due to their detrimental effects. Water bodies can get contaminated by a mix of bacteria and organic dyes, which can destroy aquatic life, especially fish as well as, flora and fauna. When animals and humans drink contaminated water, they can have a range of health issues, such as respiratory, neurological, and skin issues. Therefore, using contemporary methods to remove the dyes and

germs from the environment is imperative. A great deal of work has recently been done to investigate novel uses of photocatalysis and antimicrobials [4-7]. One practical way to get rid of the hazardous substance from the surface of the water source is to use the dye degradation process. Photocatalysis is an intriguing option for energy conversion and environmental cleanup, because of its apparent nature. Specifically, deterioration of water-containing dyes or contaminants using photocatalysis is essential for treating wastewater, since it produces no additional secondary pollutants and is inexpensive and very efficient [8-11].

In the field of photocatalysis, semiconductor photocatalysts have garnered increased interest because of their superior degrading efficiency for a range of contaminants. The distinctive features of bismuth vanadate ($BiVO_4$) with monoclinic-scheelite structure as a semiconductor photocatalyst – its smaller band gap energy such as ~ 2.4 eV, moderately good photocatalytic efficiency, acousto-optical properties, ionic conductivity, nontoxicity, chemical stability and ferroelasticity [12,13]. Recently $BiVO_4$ is thoroughly investigated, because of its capacity for use in photocatalytic processes like water splitting and pollutant decomposition when visible light is present. The applications of $BiVO_4$ in photocatalysis (like water splitting and the breakdown of pollutants when exposed to visible light) have recently drawn a great deal of research attention. An important factor influencing the properties of $BiVO_4$ is its crystal phase. Three primary crystalline phases found in $BiVO_4$ are tetragonal scheelite (ts), monoclinic scheelite (ms), and tetragonal zircon (tz). Because of its tiny energy of band gap (2.4 eV), the monoclinic scheelite structure has been shown to have the best photocatalyst among the crystals of $BiVO_4$. Thus, it is critical to regulate the crystal phase of $BiVO_4$ with ease in order to investigate its intriguing strong phase-dependant features and produce a visible-light-driven catalyst with high photocatalytic activity [14]. $BiVO_4$ photocatalytic effectiveness is limited by carriers of photo-excited charges recombine quickly, inadequate electrical conductivity, and restricted surface area and adsorptive capacity. $BiVO_4$ crystallites have been created by utilizing a range of methods, such as solid-state processes, hydrothermal processes, aqueous processes, co-precipitation method and sonochemical approach, etc. Among these, the conventional co-precipitation method is used in this work since it is an easy, affordable and surfactant-free method for the synthesis of $BiVO_4$ nanoparticles.

Photocatalytic materials are typically expected to possess strong antibacterial qualities because of their capacity for reactive oxygen species or ROS generation [15, 16]. Furthermore, in light of the future viability of devices, materials with a wide range of uses are prioritized. In this sense, $BiVO_4$ is the subject of extensive investigation because it is a substance that is safe for human cells while also possessing an ability to combat the pathogenic microorganisms. Additionally, for a material to be a superior photocatalyst, it must almost entirely cover the visible spectrum of the sun. Monoclinic $BiVO_4$ microspheres has superior photocatalytic activity compared to its tetragonal equivalent. $BiVO_4$ exhibits increased electron-hole separation when it phases out of its tetragonal structure and into a monoclinic form at 500 °C. This decreases recombination rates, hence improving the material's efficacy in degrading contaminants such as methylene blue under sunlight exposure. The phase transition influences the bandgap and optical characteristics of $BiVO_4$, enhancing its responsiveness to visible light. This enables the material to more effectively use sunlight for photocatalysis, enhancing its energy efficiency and environmental sustainability for applications such as water treatment or pollutant degradation. The phase change further augments the antibacterial activities of $BiVO_4$. Because of its altered surface structure and electrical properties, the monoclinic phase interacts with bacterial cell walls more effectively and produces more reactive oxygen species (ROS), which are essential for antibacterial activity. $BiVO_4$@500 °C is very efficacious against microorganisms that are both gram-positive and gram-negative. The best band location for the $BiVO_4$ to gather visible spectrum from solar radiation helps with its antimicrobial properties. Therefore, $BiVO_4$ nanoparticles will concurrently remove the contaminants from the water, even in the presence of infectious microbes or organic dye molecules. Their potent antibacterial activity will make it much easier to use photocatalytic $BiVO_4$ nanoparticles for continuous and frequent water cleaning. However, there have been very few studies conducted on the antibacterial properties of $BiVO_4$ nanoparticles. This inspires us to synthesize $BiVO_4$ nanoparticles and explore their dye-degradation capabilities and antibacterial efficiency [17-20].

The article presents a facile co-precipitation method for synthesizing $BiVO_4$ microspheres. The study primarily focused on the impact of temperature on the microstructural development and growth of $BiVO_4$ microspheres. Methylene blue (MB), an active non-biodegradable dye, was employed to assess the photocatalytic properties. The chemical stability and recycling efficacy of the synthesized m-$BiVO_4$ microspheres as a photocatalyst were further examined effectively in visible light. Additionally, this catalyst was used to combat gram-positive (*B. subtilis, S. aureus*) and gram-negative (*E. coli, P. vulgaris*) bacteria with its antibacterial activity.

2. Experimental

2.1. Materials

Bismuth nitrate pentahydrate ($Bi(NO_3)_3.5H_2O$), ammonium metavanadate (NH_4VO_3), sodium hydroxide (NaOH), nitric acid (HNO_3), ethanol and deionized water was obtained commercially. The Methylene blue is also

known as 3, 7- bis(dimethylamino)- phenothiazine – 5-ium chloride or tetramethyl thionine was acquired from S.D. Fine chemicals. Without carrying out any extra purification, all of the reagents were used. Millipore water was utilized throughout the investigation.

2.2. Experimental Procedure

The simple co-precipitation approach was utilized to prepare $BiVO_4$ nanoparticles. In this process, 30 milliliters of nitric acid solution were used to dissolve 0.1 mol of Bi $(NO_3)_3.5H_2O$. In addition, 30 minutes of stirring resulted in a complete dissolution of 0.1 mol of NH_4VO_3 in a NaOH solution (30 mL). The two solutions were then combined while stirring. The combined solution was kept at 50 °C and stirred for an hour. The resultant yellow precipitate was filtered and washed several times using ethanol and deionized water. It is then dried for five hours at 60°C. The as-synthesized sample was then heated for three hours at 200 °C, 300 °C, 400 °C and 500 °C temperatures using the high-temperature muffle furnace. Figure. 1 schematically illustrates the synthesis of $BiVO_4$ nanoparticles.

2.3. Characterization

The powder X-ray diffraction (XRD) using a Shimadzu XRD 6000 X-ray diffractometer with Cu Kα irradiation (λ = 1.5406 Å) was used to determine the crystallinity and phase purity of $BiVO_4$ microspheres. The sample's shape and structure were examined using a scanning electron microscope (SEM, JEOL JSM 6390) equipped with an energy-dispersive X-ray spectrometer. The microstructure was examined using transmission electron microscopy (HR-TEM, JEOL JEM 2100). X-ray photoelectron spectroscopy (XPS) studies were conducted with the PHI 5300 to identify surface elements. The functional groups on the material's surface were examined using Raman spectroscopy (WiTec alpha 300, Germany). Collect diffuse reflectance spectra and determine the band gap using a UV-Vis spectrophotometer (JASCO V-770). The photoluminescence (PL) spectra were analysed at room temperature using a HORIBA Fluoromax-4 spectrophotometer.

2.4. Measurement of Photocatalytic Activity

Under natural sunlight, we tested the produced $BiVO_4$ microsphere's photocatalytic activity using methylene blue (MB) degradation. Combine 50 mg of a photocatalyst with 100 milliliters of aqueous solution of MB (10 mg/L) and keep stirring continuously with a magnetic stirrer. To achieve an adsorption-desorption equilibrium between the MB dye molecule and the photocatalysts (bismuth vanadate nanoparticles), the suspension was stirred for half an hour in the dark before being exposed to sunlight. Every thirty minutes intervals, the irradiated MB dye solution were routinely taken from the sun light irradiation and the $BiVO_4$ microspheres that had been disseminated was extracted using centrifugation. The instrument utilized was a UV-vis spectrophotometer to examine clear, translucent solution. In order to find the MB concentration in the solution, the absorbance area at a functional wavelength was used in conjunction with the irradiation period. Catalyst stability was assessed by applying the same breakdown process repeatedly. The MB solution absorbance was evaluated using the results from the UV-Vis analysis and the efficiency of MB degradation was subsequently computed. The following equation (Equation 1) describes how well MB solution degrades when a photocatalyst is present.

$$\eta = \frac{C_0 - C_t}{C_0} \times 100\% \quad (1)$$

Where C_0 and C_t, respectively, stand for the solution's absorbance at the start of the procedure (t = 0) and at a specific time point.

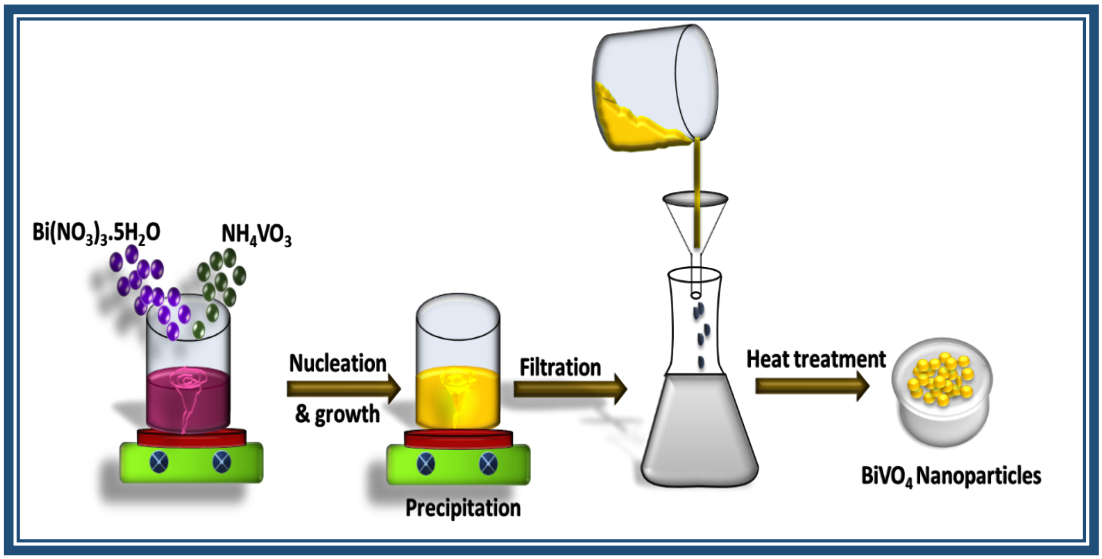

Figure 1. Schematic illustration of the synthesis of $BiVO_4$ nanoparticles

2.5. Antibacterial Studies

We tested the antibacterial efficacy of $BiVO_4$ nanoparticles at various annealing temperatures against *S. aureus*, *B. subtilis*, *E. coli* and *P. vulgaris* microorganisms. We assessed the antibacterial effectiveness of the synthesized $BiVO_4$ with 4 separate quantities (25, 50, 75, and 100 µg/mL) using the agar well diffusion technique. We independently swabbed each bacterial pathogen onto sterile Muller-Hinton agar (MHA) in individual petri plates. We made five wells with a diameter of 6 mm in the agar medium. A conventional antibiotic fills one well, while produced nanoparticles at various concentrations fill the other four. This work uses streptomycin, a common antibiotic, as a positive control. For a full day, we incubated the sample at 37 °C and determined the values of the inhibition zone in millimeters. The sample's antibacterial activity is indicated by the zone of inhibition (ZOI) surrounding the well. If the inhibition zone or ZOI around the well is higher, the sample will exhibit higher levels of antibacterial activity.

3. Results and Discussion

3.1. Structural Analysis

The phase structure of the prepared samples was characterized using X-ray diffraction studies. The XRD pattern of the synthesized $BiVO_4$ nanoparticles at various annealing temperatures is seen in Figure 2. The $BiVO_4$@500 ºC sample's XRD pattern was primarily within the monoclinic phase, which is distinguished from other phases by its strong photocatalytic activity. It is evident that all of the diffraction peaks that were found for the as-synthesised $BiVO_4$ microspheres matched those of the tetragonal $BiVO_4$ with JCPDS card No. 14-0133 [14, 21]. The diffraction peaks of $BiVO_4$@500 ºC correspond to (101), (013), (004), (200), (020), (211), (105), (123), (024), (220), (116), (303) and (132) planes of monoclinic scheelite $BiVO_4$. There were no other phase or contamination peaks found. Every peak seen in the $BiVO_4$ at 500 °C sample was indexed with the $BiVO_4$ monoclinic phase with JCPDS Card No. 83-1699, while the peaks of tetragonal $BiVO_4$ entirely vanished [13]. The most significant reflections of the monoclinic $BiVO_4$ structure were detected at 28.6°, while the tetragonal $BiVO_4$ structure's major diffraction peak was recorded at 24º. These observations led to the conclusion that the precursor initially formed into powders of tetragonal $BiVO_4$, which were thereafter progressively transformed into monoclinic $BiVO_4$ by increasing annealing temperature [22]. Additionally, it was discovered that the preparation method used in this study to create $BiVO_4$ was sensitive to the annealing temperature. These findings showed that when pure monoclinic $BiVO_4$ was formed under co-precipitation synthesis, a phase transition from the tetragonal to the monoclinic phase occurred. Consequently, it is clear that the annealing temperature had a significant role in controlling the phase structure of bismuth vanadate powder during the co-precipitation synthesis.

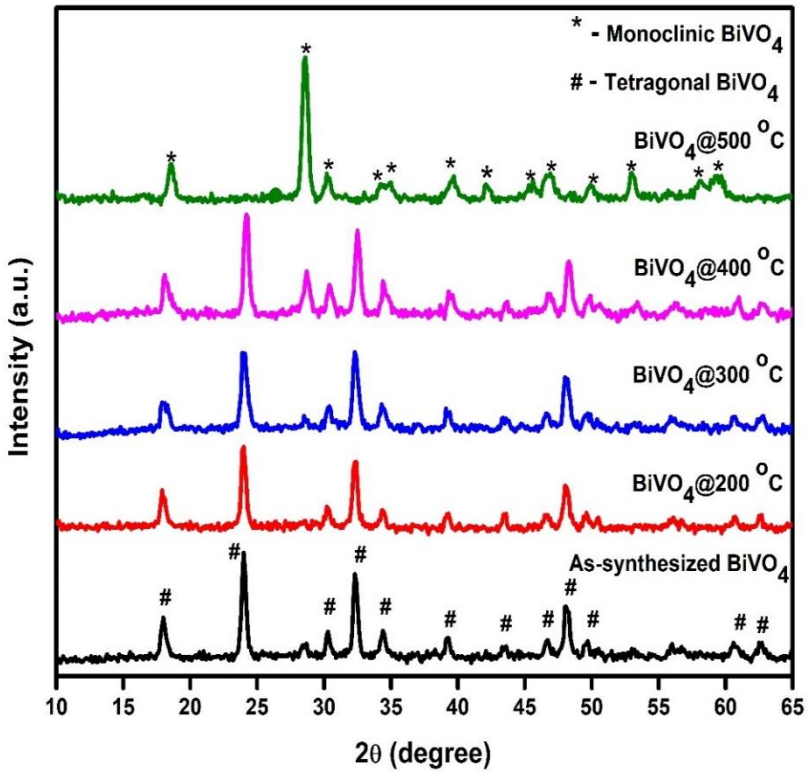

Figure 2. XRD patterns of the as-synthesized and thermally annealed $BiVO_4$.

The annealing temperature significantly affects the crystallinity, XRD patterns, and phase change of $BiVO_4$. From 200 to 500 °C, the $BiVO_4$ microspheres changes from the tetragonal phase of $BiVO_4$, which has moderate crystallinity, to the highly crystalline monoclinic phase. This change is essential in order to maximize the $BiVO_4$ potential for uses like photocatalysis toxic pollutant removal. The tetragonal phase is the most common, and $BiVO_4$ shows poor crystallinity at low temperatures. An increase in temperature brings about an improvement in crystallinity and a phase shift to the monoclinic form, greatly enhancing the $BiVO_4$ material's functionality. To change $BiVO_4$ for certain uses, like photocatalytic pollution degradation and antibacterial activity, it is important to understand these changes that happen when the temperature changes.

3.2. SEM-EDS analysis

The $BiVO_4$ nanoparticles were inspected using SEM to ascertain the morphology of the samples. Figure. 3(a-e) displays SEM images of the prepared samples that were annealed at various temperatures. All samples have granular morphology and the particles are uniformly distributed [23]. Although the particles are distinguishable. Examining the images closely reveals notable variations between the various samples. At 200 °C, the surface morphology of $BiVO_4$ at this low annealing temperature often exhibits uneven, diminutive, and indistinct particles. The substance may possess a semi-crystalline structure characterized by agglomerated microspheres. The particles are weakly aggregated and have irregular surfaces, indicating that there is insufficient energy for the formation of well-defined crystal formations. The temperature is rising, at that point, the heat energy is sufficient to encourage slight grain growth, leading to a slight rise in particle size. The surface attains a smoother texture, and the particles exhibit distinctly spherical forms. The increase in particle size is linked to improved crystallinity. The material exhibits reduced surface flaws, and the interfaces between particles are more pronounced. At 500 °C, the $BiVO_4$ particles experience further grain development and coarsening. The morphology has a highly crystalline structure characterized by larger, well-defined particles (Figure. 3e). The particles may have monoclinic formations, and the surface becomes more refined because there are fewer flaws. As the aggregate particle size increases, attributes such as photocatalytic efficacy are enhanced. The compositional investigation of $BiVO_4$ microspheres was conducted using EDS. Figure. 4(a-e) illustrates the EDX spectra of $BiVO_4$ microspheres (heat-treated at 200 °C, 300 °C, 400 °C and 500 °C samples respectively), verifying that oxygen (O), vanadium (V), and bismuth (Bi) are present. The absence of other components demonstrates the purity of the prepared microsphere. The inset of Figure. 4 illustrates the weight and atomic percentage of the component elements (Bi, V, and O) in the $BiVO_4$ microspheres that were synthesized.

3.3. HR-TEM analysis

Figure. 5 displays HR-TEM images of microspheres of $BiVO_4$ synthesized at 500 °C using the co-precipitation method. The spherical shape of $BiVO_4$ microspheres that have been annealed at 500 °C is usually clearly visible in transmission electron microscopy images. The nanoparticles are able to combine and create more homogenous microspheres when annealed at this temperature because it releases enough thermal energy. In typically, the microspheres' porous structure is the result of annealing-induced fusion of smaller nanoparticles.

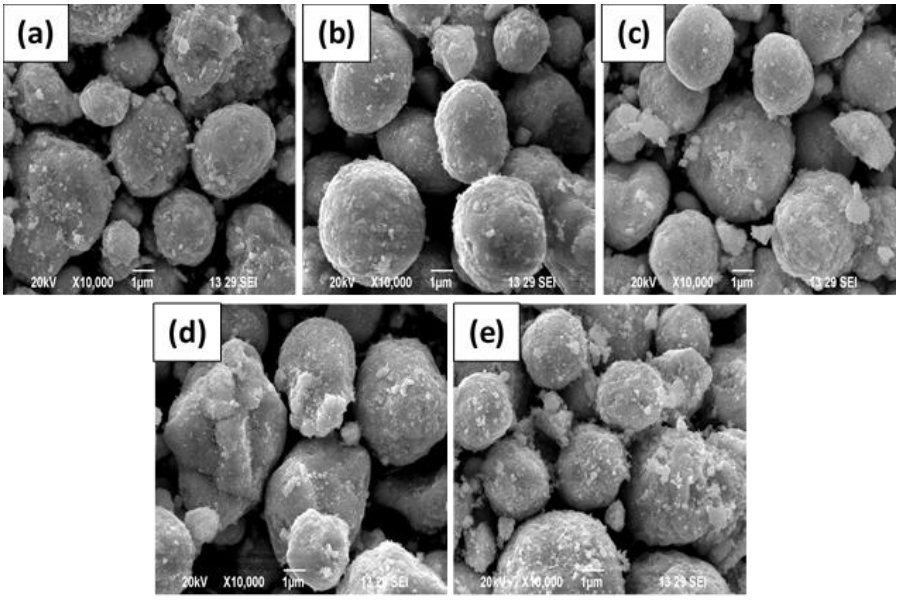

Figure 3. SEM images of **(a)** as-synthesized $BiVO_4$, **(b)** $BiVO_4$@200 °C, **(c)** $BiVO_4$@300 °C, **(d)** $BiVO_4$@400 °C and **(e)** $BiVO_4$@500 °C.

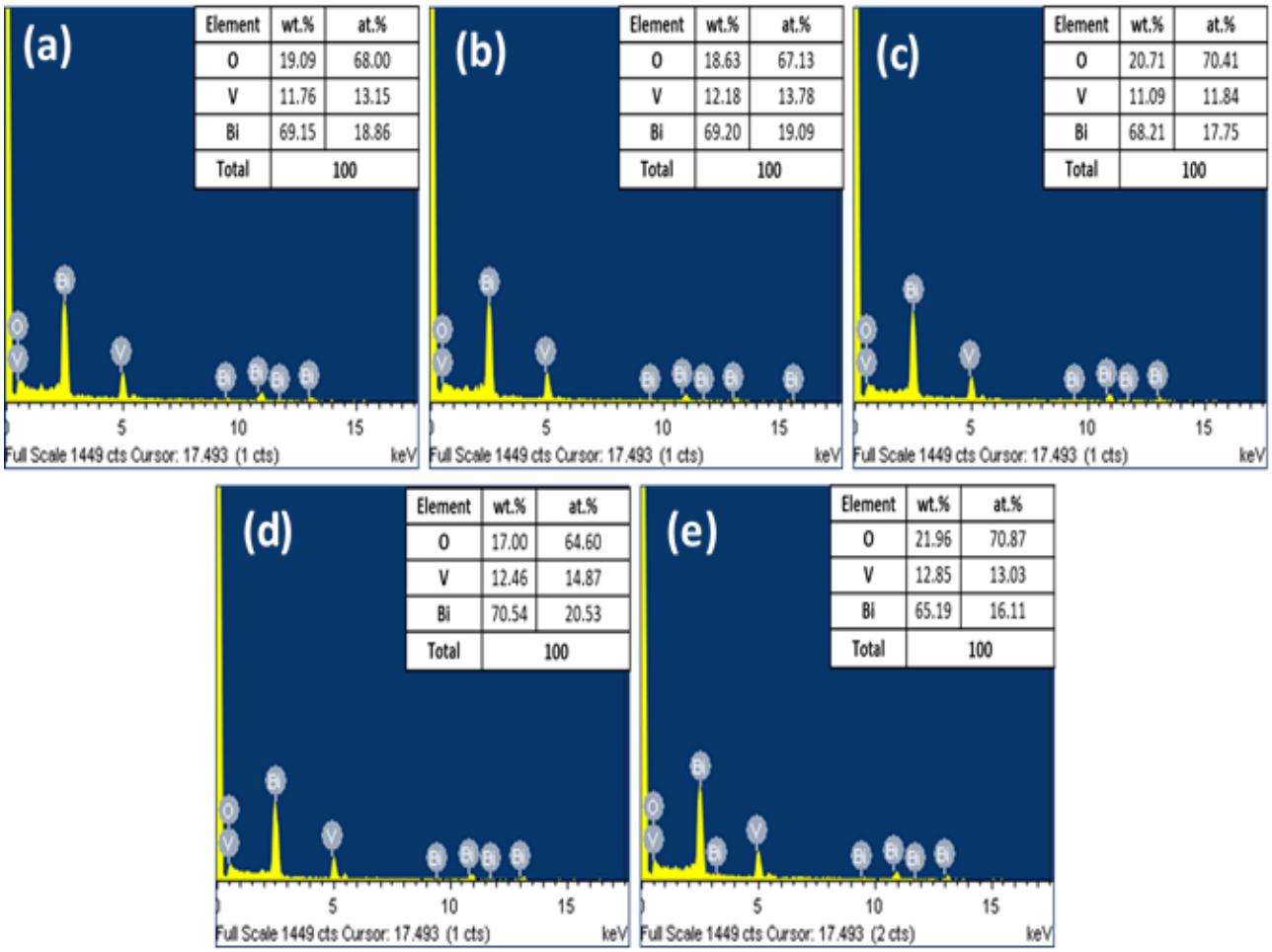

Figure 4. EDX spectra of **(a)** as-synthesized $BiVO_4$, **(b)** $BiVO_4$@200 °C, **(c)** $BiVO_4$@300 °C, (d) $BiVO_4$@400 °C and **(e)** $BiVO_4$@500 °C.

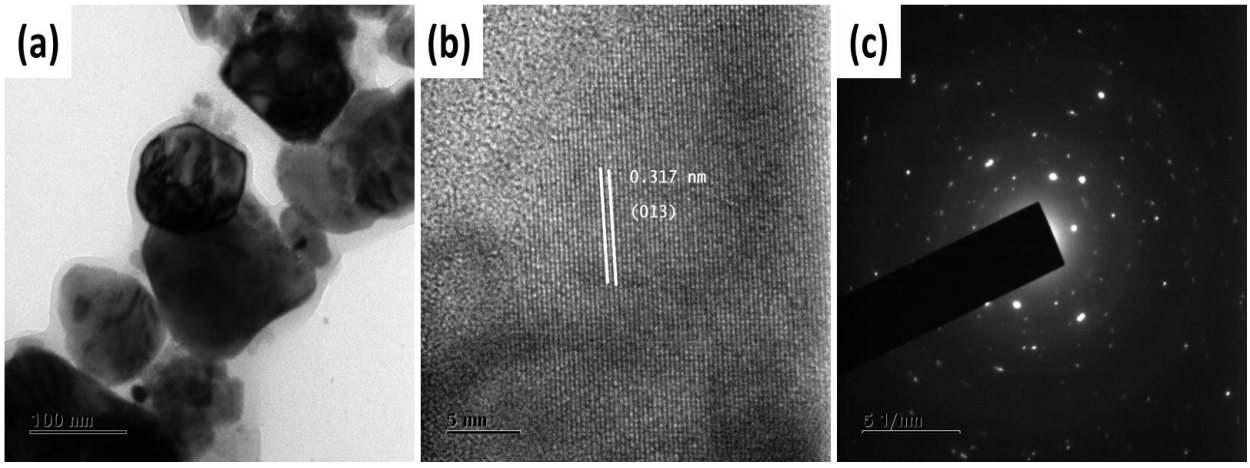

Figure 5. (a,b) HR-TEM images and **(c)** SAED pattern of $BiVO_4$@500 °C

For uses like photocatalysis, the microspheres porous structure is essential since it increases the material's contact with reactants (such dyes or pollutants). The high annealing temperature is directly responsible for the extremely crystalline nature of the individual nanoparticles. Particles have enough energy to rearrange into a highly ordered structure at 500 °C, resulting in the creation of microspheres with good crystallization. The HR-TEM images demonstrated that the particles had granular morphology. As seen in the enlarged HR-TEM picture in Figure. 5(b), there is a spacing of 0.317 nm between the crystals, which is the same as the (013) planes of monoclinic $BiVO_4$. HRTEM images frequently display lattice fringes with d-spacing that align with the monoclinic phase of $BiVO_4$, the thermodynamically stable phase at this temperature

(500 °C). Better photocatalytic activities are made possible by the unique crystal structure of $BiVO_4$'s monoclinic phase. HRTEM images emphasize the existence of grain boundaries between neighboring nanoparticles. When the nanoparticles aggregate during the annealing process, the boundaries emerge. The smoothness and sharpness of the lattice fringes in HRTEM show that each nanoparticle has a high level of crystallinity. This is needed for $BiVO_4$ to work better as a photocatalyst. Even though the nanoparticles have very high crystallinity, HRTEM may also show that they have grain boundaries and some flaws, such as dislocations or stacking faults. These flaws often occur in materials produced by high-temperature annealing and may affect the material's electrical characteristics by serving as trap sites for charge carriers. The findings unequivocally validate the monoclinic crystal structure of $BiVO_4$ @500 ºC microsphere. As presented in Figure. 5(c), the SAED ring pattern of nanoparticles absorbed in the given region electron diffraction indicated that the microsphere was polycrystalline, with multiple diffraction peaks confirming this [24]. The electron diffraction pattern contains bright spots and continuous dots indicating that the material that has been treated has a high degree of crystallinity.

3.4. XPS Analysis

X-ray photoelectron spectroscopy (XPS) was utilized to examine the surface composition and chemical states of $BiVO_4$@500 ºC (Figure. 6). Metal ion spin-orbit splitting in 2 distinct states is displayed differently by the XPS, which means they have different binding energies. The monoclinic $BiVO_4$ contains the components Bi, O, and V, based on XPS survey spectrum (Figure. 6(a)). At 285.08 eV, the C 1s signal was caused by an accidental carbon in the XPS instrument [25]. The distinctive doublet peaks, often seen as Bi $4f_{7/2}$ and Bi $4f_{5/2}$ peaks, are due to the splitting of spin-orbit and may be seen in the Bi 4f spectrum of $BiVO_4$@500 °C. Then these peaks represent bismuth in its 3+ oxidation state (Bi^{3+}).

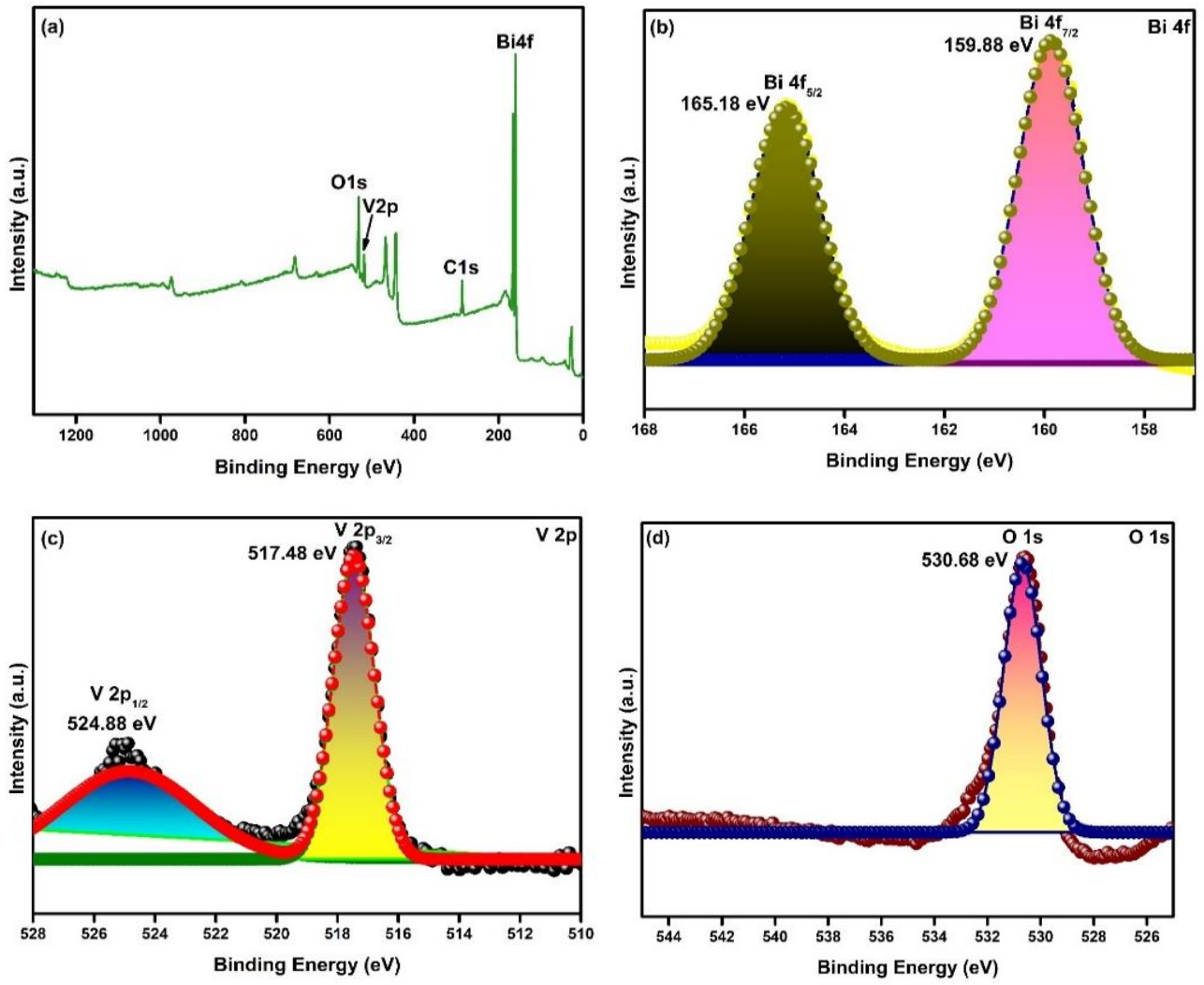

Figure 6. (a) XPS survey spectra of $BiVO_4$@500 °C; High resolution XPS spectra of (b) Bi4f, (c) V2p and (d) O1s.

The surrounding chemical environment influences the precise locations of the binding energies, which may undergo slight changes due to factors such as the material's crystallinity or its interactions with other elements. The Bi 4f 's high-resolution XPS spectrum (Figure. 6(b)) shows doublets of binding energy peaks with binding energies of 165.18 eV and 159.88 eV. These relate to Bi $4f_{5/2}$ and Bi $4f_{7/2}$, respectively. The two binding energies differ by 5.3 eV, suggesting that the oxidation state of bismuth is +3. The HRXPS of the V 2p spectrum shows a doublet, with peaks at V $2p_{3/2}$ and V $2p_{1/2}$. These peaks in the data show that the oxidized V state of vanadium stays the same in $BiVO_4$@500 °C. This is an important part of the material's photocatalytic activity because it affects its electronic structure and its capacity to make ROS, or reactive oxygen species.

However, the split V2p peaks in Figure. 6(c) at 524.88 eV and 517.48 eV, respectively, are associated with V $2p_{1/2}$ and V $2p_{3/2}$. This shows that the oxidation state of vanadium in $BiVO_4$ is +5 [26, 27]. Figure. 6(d) shows the O 1s spectrum typical with 530.68 eV as the prominent characteristic peak. Thus, per the XRD and XPS results further confirmed that the sample consisted of $BiVO_4$ [28].

3.5. Raman Analysis

The structure of the samples was subsequently analyzed using Raman spectra, a sensitive tool for studying structural changes. Through increasing the annealing temperature, Raman spectroscopy helps facilitate the change in phase from tetragonal to monoclinic. Figure. 7(a) displays the Raman spectra of the $BiVO_4$ microspheres at various annealing temperatures. The mode of symmetrical V-O stretching of the monoclinic and tetragonal phases is represented by the peaks in the $BiVO_4$ spectra at 830 and 858 cm^{-1}, respectively. Weak peak at 709 and 760 cm^{-1} were caused by asymmetric stretching of the V-O bond for monoclinic and tetragonal phases respectively. According to the VO_4^{3-} tetrahedron, the asymmetric and symmetric deformation modes are associated with Raman bands at 330 and 370 cm^{-1}, respectively. The vibration (external mode) of the monoclinic phase is shown by peaks at 218 and 131 cm^{-1} belonging to surface vibration. However, the tetragonal phase (external mode) is thought to be the cause of the 250 cm^{-1} peak [29].

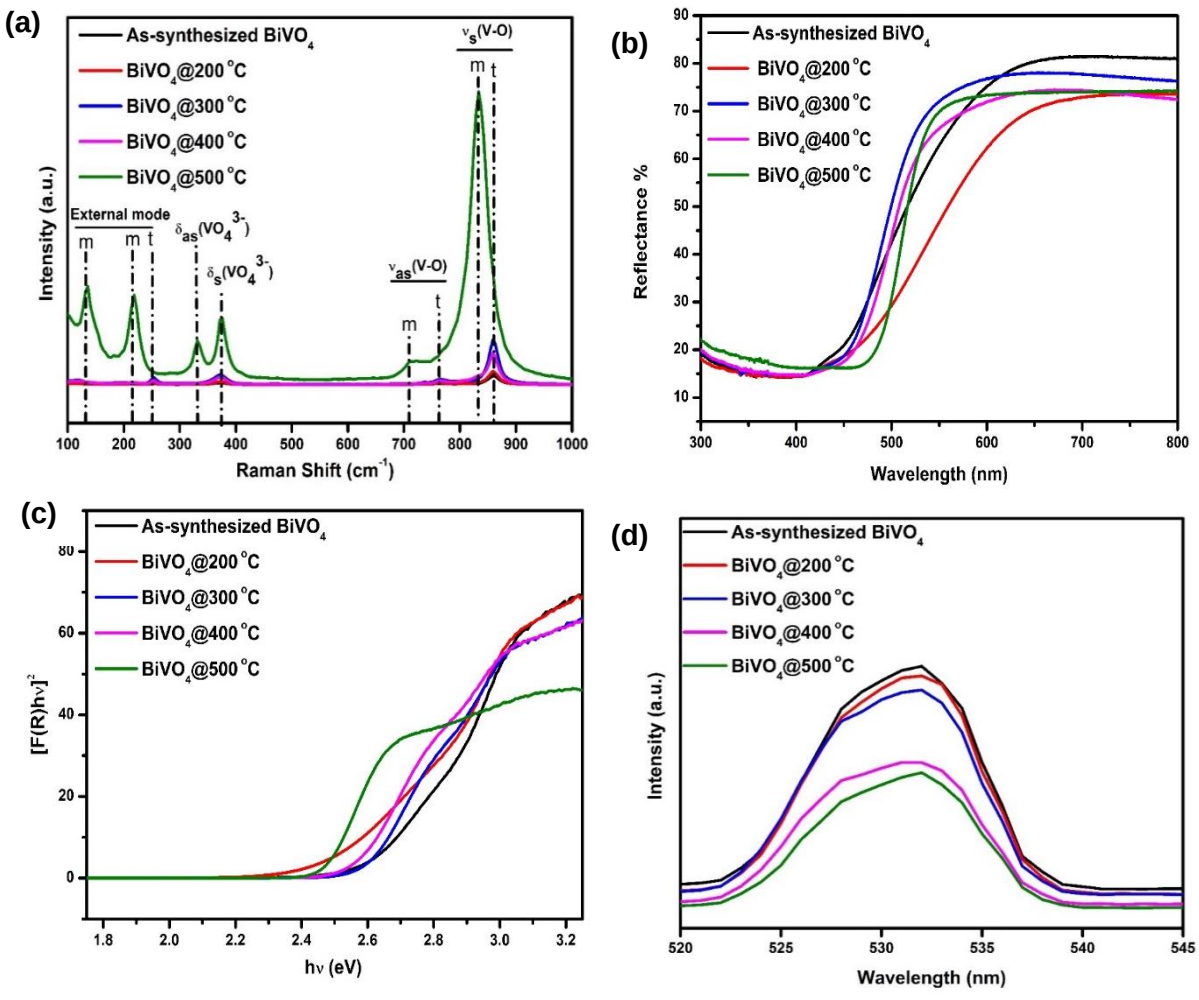

Figure 7. (a) Raman spectra **(b)** UV-Vis diffuse reflectance spectra, **(c)** Kubelka-Munk plot, **(d)** Photoluminescence spectra of as-synthesized and thermally annealed $BiVO_4$.

The Raman spectral analysis strongly verified phase transition from tetragonal to monoclinic by demonstrating that the $BiVO_4$@500 ºC sample did not have peaks at 250, 760, or 858 cm^{-1}.

3.6. UV-Vis DRS Analysis

UV-vis DRS method was used for determining the photocatalyst's optical band gap energy. One useful method to assess semiconductor material's optical characteristics, which are believed to be critical to photocatalytic performance is diffuse reflectance spectroscopy. As part of an examination of the optical properties, the UV-vis diffuse reflection spectra of five $BiVO_4$ samples at different annealing temperatures are shown in Figure. 7(b). F(R) can be calculated from the reflectance data to obtain the band gap values and Fig. 7(c) displayed the $[F(R).hu]^2$ against energy of photon (hu) plot. The formula for Kubelka-Munk function (F(R)) is (Equation 2),

$$F(R) = \frac{(1-R)^2}{2R} \quad (2)$$

where R represents, the measured diffuse reflectance [30].

It is discovered that the band gap energy of as-synthesized $BiVO_4$ is found to be 2.801 eV. After annealing the $BiVO_4$ microspheres at 200 °C, 300 °C, 400 °C, and 500 °C, the band gap values obtained are 2.687, 2.591, 2.512, and 2.434 eV, respectively. It is evident that when the annealing temperature increases up to 500 °C, the band gap reduces. Changes in the annealing temperatures could account for the variations in the optical band gap energy. These changes in samples thus determine the degree of delocalization of photogenerated electron and hole pairs [31]. The variations in band gap energy indicate that the $BiVO_4$ microsphere sample's electronic structures undergo changes as the temperature of the heat treatment varies. These changes in the electronic structures cause photogenerated carriers to delocalize to different degrees, which means that the samples have different mobility efficiencies [22, 29].

3.7. PL Analysis

Figure. 7(d) displays the photoluminescence (PL) emission spectra of $BiVO_4$ at various annealing temperatures. PL spectra can help us understand how the photogenerated charge carriers (electron-hole pairs) in $BiVO_4$ semiconductor materials can move, transfer, and recombine together. The PL emission peak intensity correlates with the recombination of photogenerated electrons and holes. $BiVO_4$ microspheres heated to 500 °C have a very low emission peak intensity compared to other samples. This indicates a highly efficient separation of photogenerated charge carriers. Thus, this substance has favorable properties for use in photocatalytic processes. However, the synthesized $BiVO_4$'s higher luminescence intensity suggests that defects caused by charge recombination were making the photocatalytic process less effective [32, 33].

3.8. Photocatalytic Activity

The photocatalytic activity of $BiVO_4$ microspheres at various annealing temperatures was assessed by means of the MB aqueous solution's deterioration. The photocatalytic results are shown in Figure. 8. It is crucial to note that $BiVO_4$@500 °C microspheres have greater photocatalytic activity than $BiVO_4$ at other temperatures when subjected to sunlight irradiation. The $BiVO_4$@500 °C microspheres degrade MB to 83.25% after 120 minutes of irradiation, while as-synthesized, $BiVO_4$@200 °C, $BiVO_4$@300 °C and $BiVO_4$@400 °C microspheres degraded MB to 71.74%, 73.55%, 76.67% and 77.83% respectively (Figure. 8(c)). Since annealing temperature increased by 500 °C, the charge carriers that were photogenerated in the monoclinic phase were effectively separated, which is responsible for the rise in photocatalytic degradation effect. Moreover, the UV-vis DRS confirm that annealing temperature can reduce $BiVO_4$'s band gap and maximize sunlight absorption, resulting in improved photocatalytic dye degradation efficiency [29].

3.9. Kinetic Study

Using Langmuir–Hinshelwood kinetic model (L-H kinetic model), photocatalytic efficiency of $BiVO_4$ nanoparticles annealed with various temperatures was studied for the breakdown of MB aqueous solution in the presence of sunlight irradiations (Equation 3).

$$ln\frac{C_0}{C_t} = kt \quad (3)$$

Where C_0 represents the initial concentration of MB dye, although C_t denotes the dye's concentration at a particular irradiation period t, pseudo-first-order reaction theory governs the rate constant, represented as k [34]. Moreover, the subsequent equation was used to obtain $t_{1/2}$ (min) (Equation 4) [35].

$$t1/2 = 0.693/k \quad (4)$$

Figure. 8(b) represents a linear relationship between ln C_0/C_t and irradiation time t. Table 1 summarizes degradation percentage, pseudo first order rate constants k, half-life time $t_{1/2}$, and linear regression coefficients R^2. In comparison to as-synthesized $BiVO_4$, $BiVO_4$@200 °C, $BiVO_4$@300 °C and $BiVO_4$@400 °C samples, it was discovered that the value of the pseudo-first-order rate constant k was maximal (0.0151 min^{-1}), while $t_{1/2}$ was least (45.68 min) for $BiVO_4$ nanoparticles annealed at 500 °C. The findings unequivocally show that, when exposed to sunlight, an annealing temperature of 500 ºC is the ideal temperature for $BiVO_4$ nanoparticles produced by the co-precipitation process in order to maximize breakdown of MB dye by photocatalysis.

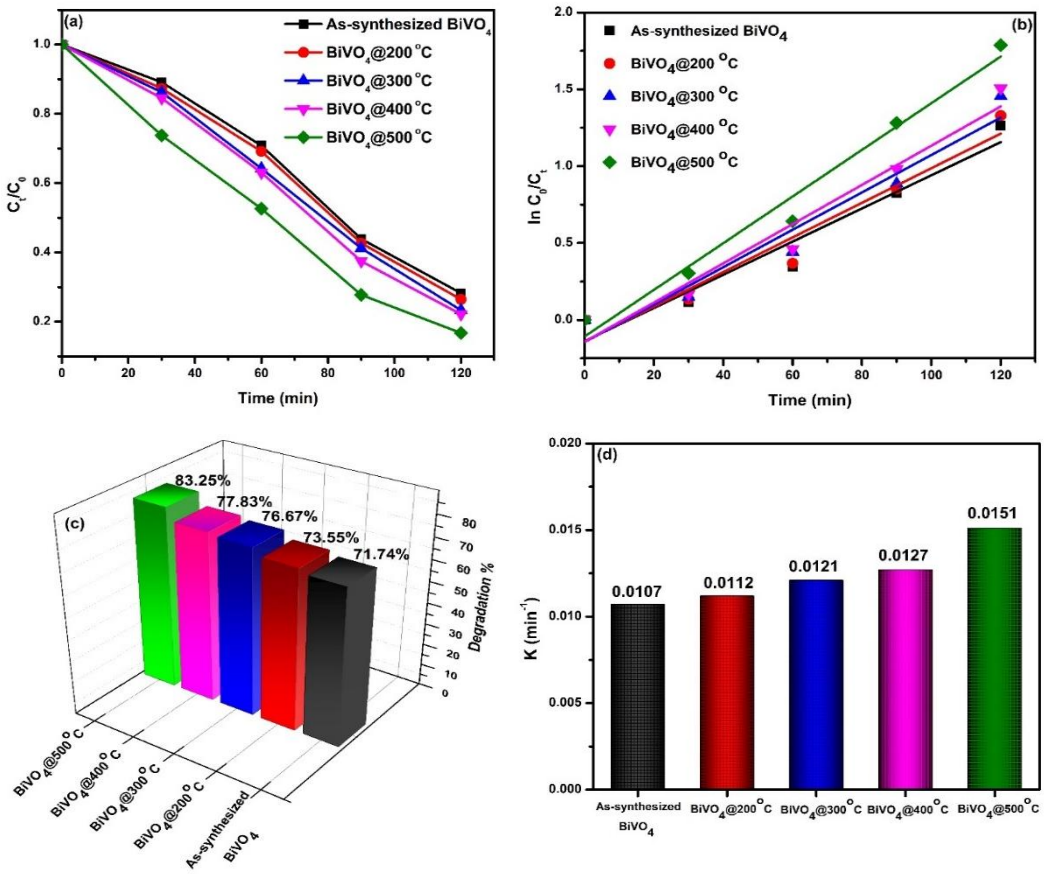

Figure 8. (a) Photocatalytic degradation curves; **(b)** Pseudo-first-order kinetics curve; **(c)** degradation efficiency; **(d)** rate constant of as-synthesized and thermally annealed $BiVO_4$ for MB dye degradation.

Table 1. Calculated band gap, pseudo-first-order rate constant (k), half-life ($t_{1/2}$), regression coefficient (R^2) and degradation efficiency of $BiVO_4$ nanoparticles.

Sample	Band gap (eV)	Rate constant k (min^{-1})	Half-life $t_{1/2}$ (min)	Regression coefficient R^2	Degradation efficiency (%)
As-synthesized $BiVO_4$	2.801	0.0107	64.22	0.924	71.74
$BiVO_4$@200 ºC	2.687	0.0112	61.60	0.926	73.55
$BiVO_4$@300 ºC	2.591	0.0121	56.99	0.933	76.67
$BiVO_4$@400 ºC	2.512	0.0127	54.31	0.942	77.83
$BiVO_4$@500 ºC	2.434	0.0151	45.68	0.971	83.25

The photocatalytic degradation rate constants, k, of MB dye under the radiation of sunlight vary for different annealed $BiVO_4$ nanoparticles, as displayed in Figure. 8(d). It is apparent from the bar diagram that $BiVO_4$ nanoparticles annealed at 500 ºC yield the largest value of k. When compared to the other four samples, $BiVO_4$@500 °C with k value is 1.4 times higher. So, the rate of MB degradation over the $BiVO_4$@500 °C nanoparticles is significantly faster than that of the other samples. The obtained R^2 values for as-synthesized $BiVO_4$, $BiVO_4$@200 °C, $BiVO_4$@300 °C, $BiVO_4$@400 °C and $BiVO_4$@500 °C nanoparticles are 0.924, 0.926, 0.933, 0.942 and 0.971 respectively, in turn, suggested that the L-H model could accurately predict the photocatalytic data. Additionally, the R^2 values are above 0.9, indicating a very good fit.

3.10. Stability and reusability of $BiVO_4$@500 °C

An effective catalyst can be reused multiple times while maintaining nearly the same efficiency, as demonstrated by its reusability. Examining the synthesized catalyst's potential for reuse is therefore crucial from a practical standpoint. To evaluate $BiVO_4$@500 °C's capacity to be reused for the photodegradation of the MB dye, five cycle tests were

carried out (Figure. 9(a)). Results show that degradation performance drops from 83% to 80% even after five cycles. The investigations demonstrate and validate $BiVO_4$@500 °C nanoparticle's effectiveness as a photocatalyst due to its high reusability. Moreover, we carried out XRD analysis following the photocatalytic process to confirm the stability, as illustrated in Figure. 9(b). Further evidence that this catalyst is sufficiently stable for reuse comes from the fact that, following the degradation experiment, the XRD spectrum of the $BiVO_4$@500 °C sample did not noticeably change when compared to the unused sample. This sample, therefore, not only shows a good rate of degradation but also a high degree of stability and recyclability.

3.11. Photocatalytic Mechanism

Figure 10 shows a possible mechanism via which $BiVO_4$ microsphere photocatalysts could destroy MB through photocatalysis. Photoinduced electron transfers (e^-) traversing the conduction band (CB) from the valence band (VB) in the presence of visible light irradiation, ultimately lead to the creation of photoinduced holes (h^+) in the VB. The e^- and h^+ are consequently produced in the CB and VB, respectively. Oxygen (O_2) captures electrons, leading to the formation of the superoxide anion radical or $\cdot O_2^-$, conversely, the extremely reactive hydroxyl radical ($\cdot$OH) can be developed when photogenerated holes contact with water adsorbed on $BiVO_4$ nanoparticle's surface.

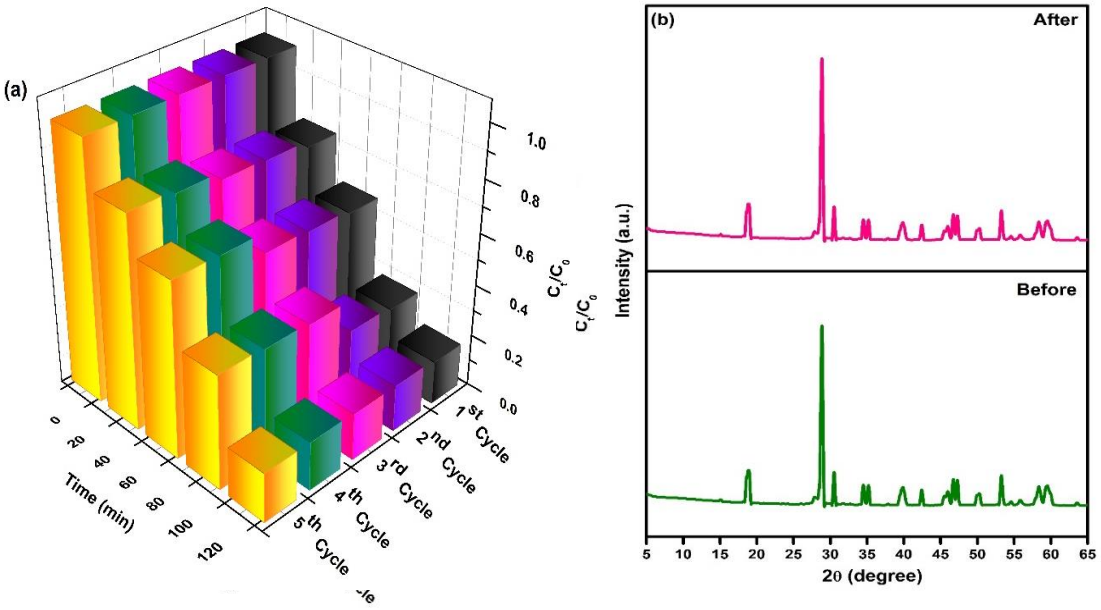

Figure 9. (a) Cyclic test; and **(b)** XRD patterns of before and after photocatalytic degradation of MB in the presence of $BiVO_4$@500 ºC

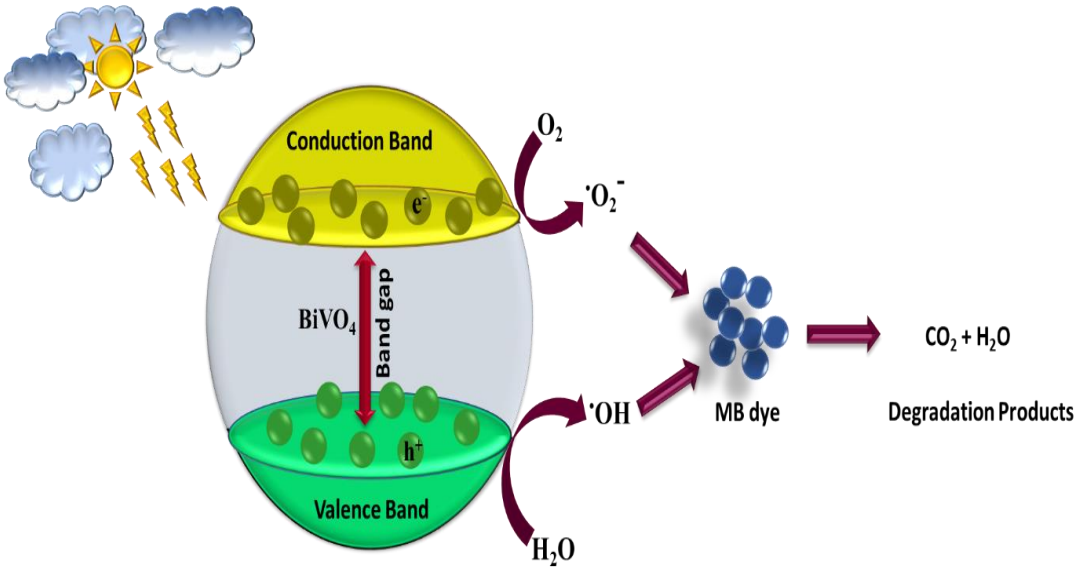

Figure 10. Photocatalytic degradation mechanism of MB dye by $BiVO_4$@500 ºC.

With their potent oxidizing power, these reactive radicals can break down the MB dye into organic molecules that are not harmful [36, 37]. The below equations (Equation 5-8) are an illustration of a potential photocatalytic reaction process for $BiVO_4$:

$$BiVO_4 + hu \longrightarrow e^- + h^+ \quad \text{-----(5)}$$

$$e^- + O_2 \longrightarrow \cdot O_2^- \quad \text{-----(6)}$$

$$h^+ + H_2O \longrightarrow \cdot OH \quad \text{-----(7)}$$

$$MB + \cdot O_2^- + \cdot OH + h^+ \longrightarrow \text{Degradation products } (CO_2 + H_2O) \quad \text{-----(8)}$$

3.12. Antibacterial Activity

The antibacterial activity of as-synthesized $BiVO_4$ and $BiVO_4$ nanoparticles at various annealing temperatures, specifically 200 °C, 300 °C, 400 °C and 500 °C was tested at various doses (25, 50, 75, and 100 µg/mL) using gram-positive: *B. subtilis, S. aureus* and gram-negative: *E. coli, P. vulgaris* microorganisms. Figure. 11(a-d) shows bar diagrams, representing the alteration in the inhibitory zone's diameter. Table 2 displays the findings the zone of inhibition (ZOI) measurement. It has been discovered that $BiVO_4$ nanoparticles at various annealing temperatures have greater antibacterial activity than those that as-synthesized. Among all of the produced products, the $BiVO_4$@500 °C had the maximum potency over *S. aureus* bacteria possessing ZOI 16 mm at a 100 µg/mL concentration. This might be due to their band gap values getting narrower. When the band gap gets smaller, there's a potential that exciton generation will happen. As a result, $BiVO_4$@500 °C nanoparticles exhibit enhanced overall photocatalytic and antibacterial characteristics. The zone of inhibition rises in tandem with an increase in sample concentrations. Under the same conditions, the two strain's differing levels of antibacterial activity could have been caused by variations in their membrane structures. Gram-negative bacteria can be distinguished from gram-positive bacteria by their outer membrane covered by a peptidoglycan layer. Considering that there are substances outside of them that have the ability to destroy germs, it also helps them survive. The study indicates that $BiVO_4$@500 °C nanoparticles are useful in biological applications [38].

3.13. Antibacterial mechanism

The intricate mechanism behind the nanoparticle's antibacterial action occurs within intercellular organelles or on the cell membrane of harmful microorganisms. The antibacterial mechanism of $BiVO_4$ nanoparticles is illustrated in Figure. 12.

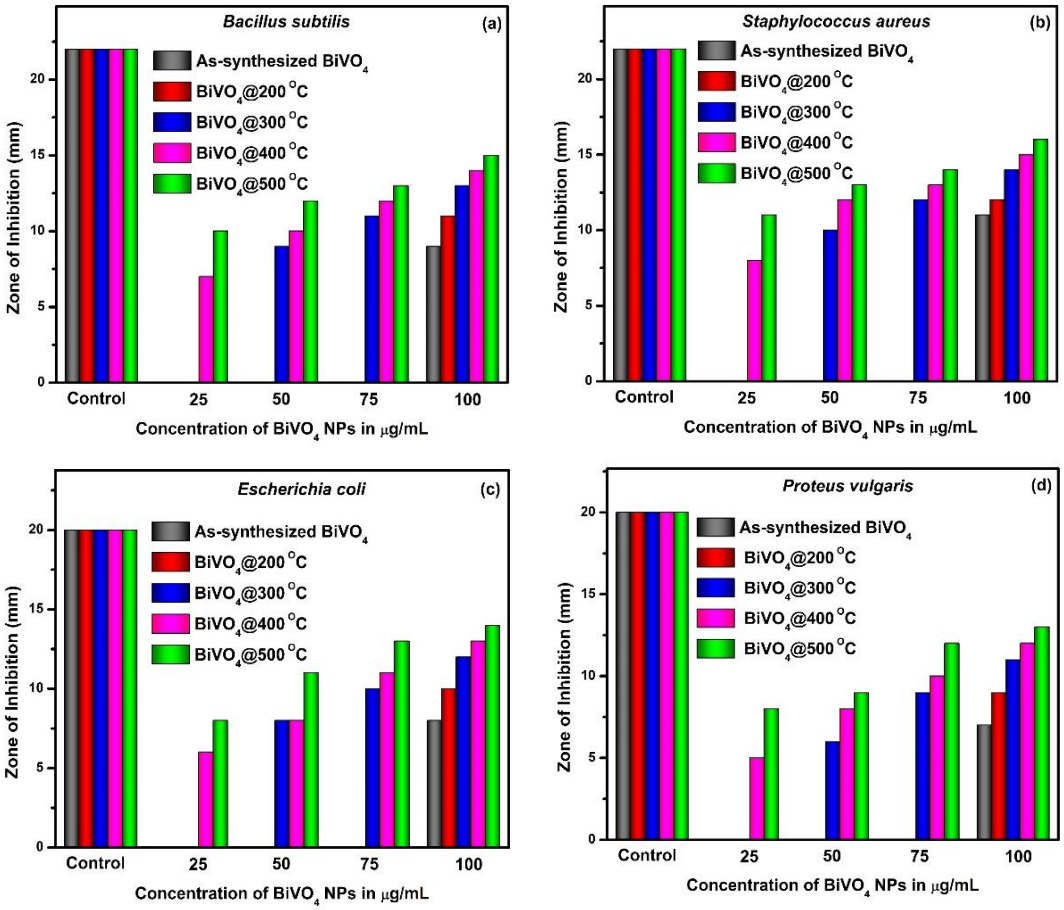

Figure11. Antibacterial activity of as-synthesized and thermally annealed $BiVO_4$ against (a) *B. subtilis*, (b) *S. aureus*, (c) *E. coli* and (d) *P. vulgaris* bacteria.

Table 2. Antibacterial activity of $BiVO_4$ nanoparticles

Sample	Zone of inhibition (mm)																			
	B. subtilis					S. aureus					E. coli					P. vulgaris				
	Control	25 µg/mL	50 µg/mL	75 µg/mL	100 µg/mL	Control	25 µg/mL	50 µg/mL	75 µg/mL	100 µg/mL	Control	25 µg/mL	50 µg/mL	75 µg/mL	100 µg/mL	Control	25 µg/mL	50 µg/mL	75 µg/mL	100 µg/mL
As-synthesized $BiVO_4$	22	00	00	00	9	22	00	00	00	11	20	00	00	00	08	20	00	00	00	07
$BiVO_4$@200 °C	22	00	00	00	11	22	00	00	00	12	20	00	00	00	10	20	00	00	00	09
$BiVO_4$@300 °C	22	00	09	11	13	22	00	10	12	14	20	00	08	10	12	20	00	06	09	11
$BiVO_4$@400 °C	22	07	10	12	14	22	08	12	13	15	20	06	08	11	13	20	05	08	10	12
$BiVO_4$@500 °C	22	10	12	13	15	22	11	13	14	16	20	08	11	13	14	20	08	09	12	13

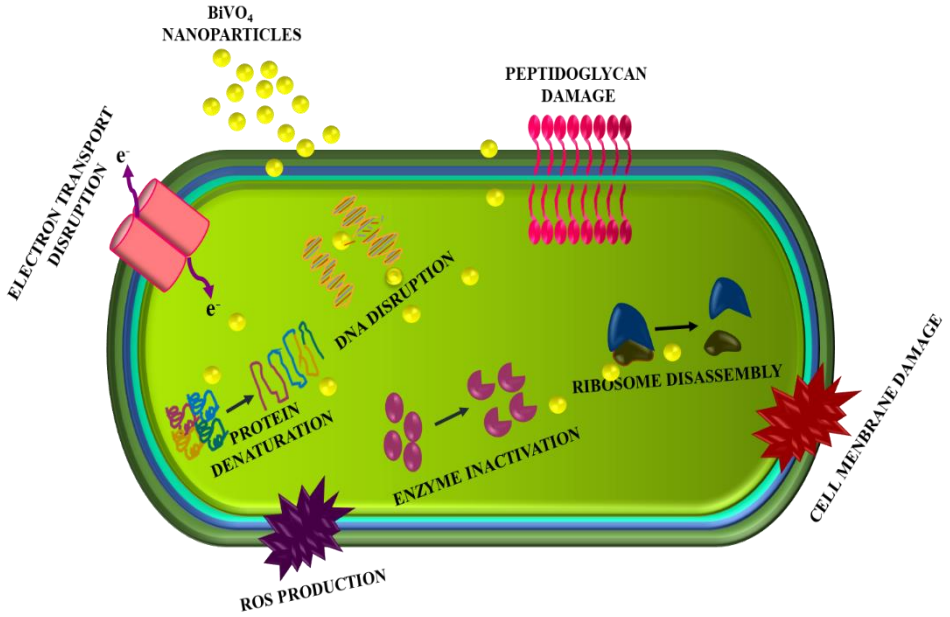

Figure 12. The antibacterial activity mechanism of $BiVO_4$ nanoparticles

Table 3. Comparative study of photocatalytic and antibacterial activity of present work with the previous reported works

Catalyst	Method of synthesis	Model Pollutant	Degradation Time	Efficiency of Degradation (%)	Studied bacteria	Antibacterial test result	Ref
$BiVO_4$	Hydrothermal	CV	120 min	98.21%	-	-	[13]
$BiVO_4$	Hydrothermal	RhB CV	210 min 120 min	64.81% 96.23%	-	-	[29]
$BiVO_4$	Microwave hydrothermal method	MB	160 min	81.6%	-	-	[40]
$BiVO_4$	Microwave	MB	300 min	75.14%	-	-	[39]
$BiVO_4$	Hydrothermal	MB	135 min	62%	*E. coli*	100%	[41]
$BiVO_4$	**Co-precipitation method**	**MB**	**120 min**	**83.25%**	***B. Subtilis*** ***S. aureus*** ***E. coli*** ***P. vulgaris***	**Maximum antibacterial activity achieved for *S. aureus* with zone of inhibition 16 mm**	**Present work**

Nanoparticles typically inhibit bacteria in four ways: (i) by causing cell wall damage; (ii) by preventing replication of DNA and the development of ROS; (iii) by preventing the production of the proteins and (iv) by causing disruption bacteria's metabolism. The size and formation of ROS are the main elements affecting the dangerous microorganism's inhibition. The usual range of sizes for bacteria is in micrometers, and their cell walls allow for the passage of minute monodispersed nanoparticles. According to UV-Vis analysis, it is evident that the $BiVO_4$@500 °C nanoparticle in this instance possesses a reduced energy of optical band gap than the other samples, which indicates that reactive oxygen species production is also higher. This could explain the outstanding ability to combat two types of bacteria such as gram-positive and gram-negative, which is quite impressive. However, a good understanding of the precise contribution of $BiVO_4$ nanoparticles to the antibacterial action is still lacking [39-41].

Table 3 is an analysis of how the current work compares with previous works that were published.

4. Conclusion

The facile co-precipitation method successfully synthesized $BiVO_4$ nanoparticles at various annealing temperatures. There had been a phase change from the tetragonal to the monoclinic phase. $BiVO_4$ exhibits microsphere morphologies as shown by SEM and HR-TEM. The circular SAED patterns confirm the polycrystalline nature of $BiVO_4$@500 °C nanoparticles. Compositional analysis verified the presence of Bi, V, and O. $BiVO_4$ at 500 °C's chemical composition has been investigated using XPS spectra, revealing the parts that are present and the binding energies that correspond to the oxidation state of elements.

We observe a decrease in the energy band gap (Eg) (2.801–2.434 eV) as the temperature increases. $BiVO_4$@500 °C exhibits the lowest PL emission intensity because of the wide charge carrier segregation, which increases photocatalytic efficiency.

The $BiVO_4$@500 °C nanoparticles demonstrated a better antibacterial activity towards both gram-positive and gram-negative bacteria. Among them, greater antibacterial activity with a 16 mm inhibitory zone is observed against bacteria *S. aureus*. Therefore, the synthesized $BiVO_4$@500 °C nanoparticles have the ability to remove pathogens and organic contaminants simultaneously from the water that was contaminated.

References

[1] M.M. Naik, H.S.B. Naik, G. Nagaraju, M. Vinuth, K. Vinu, S.K. Rashmi, Effect of aluminium doping on structural, optical, photocatalytic and antibacterial activity on nickel ferrite nanoparticles by sol–gel auto-combustion method. Journal of Materials Science: Materials in Electronics, 29, (2018) 20395–20414. https://doi.org/10.1007/s10854-018-0174-y

[2] K. Thirumalai, S. Balachandran, K. Selvam, M. Swaminathan, Nanoribbon-structured $CdWO_4$–ZnO for multiple applications. Emerging Materials Research, 5, (2016) 264–276. https://doi.org/10.1680/jemmr.15.00085

[3] S. Rajasri, B. Krishnakumar, A.J.F.N. Sobral, S. Balachandran, M. Swaminathan, I. Muthuvel, Development of $Cd_3(PO_4)_2$/rGO coupled semiconductor system for effective mineralization of basic Violet 10 (BV 10) under UV-A light. Materials Today: Proceedings, 15(3), (2019) 471–480. https://doi.org/10.1016/j.matpr.2019.04.109

[4] S. Selvinsimpson, P. Gnanamozhi, V. Pandiyan, M. Govindasamy, M.A. Habila, N. AlMasoud, Y. Chen, Synergetic effect of Sn doped ZnO nanoparticles synthesized via ultrasonication technique and its photocatalytic and antibacterial activity. Environmental Research, 197, (2021) 111115. https://doi.org/10.1016/j.envres.2021.111115

[5] T. Munawar, S. Yasmeen, F. Mukhtar, M.S. Nadeem, K. Mahmood, M. Saqib Saif, M. Hasan, A. Ali, F. Hussain, F. Iqbal, Zn0.9Ce0.05M0.05O (M = Er, Y, V) nanocrystals: Structural and energy bandgap engineering of ZnO for enhancing photocatalytic and antibacterial activity. Ceramics International, 46(10), (2020) 14369–14383. https://doi.org/10.1016/j.ceramint.2020.02.232

[6] P. Gnanamozhi, V. Renganathan, S.-M. Chen, V. Pandiyan, M. Antony Arockiaraj, N.S. Alharbi, S. Kadaikunnan, J.M. Khaled, K.F. Alanzi, Influence of Nickel concentration on the photocatalytic dye degradation (methylene blue and reactive red 120) and antibacterial activity of ZnO nanoparticles. Ceramics International, 46(11), (2020) 18322–18330. https://doi.org/10.1016/j.ceramint.2020.05.054

[7] T. Munawar, M.S. Nadeem, F. Mukhtar, M. Hasan, K. Mahmood, M.I. Arshad, A. Hussain, A. Ali, M.S. Saif, F. Iqbal, Rare earth metal co-doped Zn0·9La0.05M0.05O (M = Yb, Sm, Nd) nanocrystals; energy gap tailoring, structural, photocatalytic and antibacterial studies. Materials Science in Semiconductor Processing, 122, (2021) 105485. https://doi.org/10.1016/j.mssp.2020.105485

[8] K.P. Ghoderao, S.N. Jamble, R.B. Kale, Hydrothermally synthesized Cd-doped ZnO nanostructures with efficient sunlight-driven photocatalytic and antibacterial activity. Journal of Materials Science: Materials in Electronics, 30, (2019) 11208–11219. https://doi.org/10.1007/s10854-019-01466-y

[9] V. Beena, S. Ajitha, S.L. Rayar, C. Parvathiraja, K. Kannan, G. Palani, Enhanced photocatalytic and antibacterial activities of ZnSe nanoparticles. Journal of Inorganic and Organometallic Polymers and Materials, 31, (2021) 4390–4401. https://doi.org/10.1007/s10904-021-02053-7

[10] M.S. Nadeem, T. Munawar, F. Mukhtar, M. Naveed ur Rahman, M. Riaz, F. Iqbal, Enhancement in the photocatalytic and antimicrobial properties of ZnO nanoparticles by structural variations and energy bandgap tuning through Fe and Co co-doping. Ceramics International, 47(8), (2021) 11109–11121. https://doi.org/10.1016/j.ceramint.2020.12.234

[11] R. Dhilip Kumar, K. Sreevani, G. Radhika, V. Sethuraman, V. Shanmugavalli, S. Nagarani, S. Balachandran, M. Kumar, One-Pot synthesis of CuO-Cu2O nanoscrubbers for high-performance pseudo-supercapacitors applications. Materials Science and Engineering: B, 281 (2022) 115755. https://doi.org/10.1016/j.mseb.2022.115755

[12] A. Helal, S.M. El-Sheikh, J. Yu, A.I. Eid, S.A. El-Haka, S.E. Samra, Novel synthesis of BiVO4 using homogeneous precipitation and its enhanced photocatalytic activity. Journal of Nanoparticle Research, 22, (2020). https://doi.org/10.1007/s11051-020-04861-3

[13] Y.M. Hunge, A. Uchida, Y. Tominaga, Y. Fujii, A.A. Yadav, S. Kang, N. Suzuki, I. Shitanda, T. Kondo, M. Itagaki, M. Yuasa, S. Gosavi, A. Fujishima, C. Terashima, Visible Light-Assisted Photocatalysis Using Spherical-Shaped BiVO4 Photocatalyst. Catalysts, 11(4), (2021) 460. https://doi.org/10.3390/catal11040460

[14] N.D. Phu, L.H. Hoang, P.K. Vu, M.-H. Kong, X.-B. Chen, H.C. Wen, W.C. Chou, Control of crystal phase of BiVO4 nanoparticles synthesized by microwave assisted method. Journal of Materials Science: Materials in Electronics, 27, (2016) 6452–6456. https://doi.org/10.1007/s10854-016-4585-3

[15] M. Selvamani, A. Kesavan, A. Arulraj, P.C. Ramamurthy, M. Rahaman, S. Pandiaraj, M. Thiruvengadam, E.J. Sacari Sacari, E.M.

Limache Sandoval, M.R. Viswanathan, Microwave-assisted synthesis of flower-like MnMoO4 nanostructures and their photocatalytic performance. Materials, 17(7), (2024) 1451. https://doi.org/10.3390/ma17071451

[16] M. Selvamani, S. Balachandran, A.V. Kesavan, V. Vinoth, Bi_2MoO_6 nano-flowers for Bi-functional application: Anticancer activity against B16F10 (Mice melanoma) and photocatalytic dye degradation. Surfaces and Interfaces, 42, (2023) 103340. https://doi.org/10.1016/j.surfin.2023.103340

[17] M. Ganeshbabu, N. Kannan, P.S. Venkatesh, G. Paulraj, K. Jeganathan, D. MubarakAli, Synthesis and characterization of $BiVO_4$ nanoparticles for environmental applications. RSC Advances, 10, (2020) 18315–18322. https://doi.org/10.1039/D0RA01065K

[18] R.D. Kumar, S. Nagarani, S. Balachandran, C. Brundha, S.H. Kumar, R. Manigandan, M. Kumar, V. Sethuraman, S.H. Kim, High performing hexagonal-shaped ZnO nanopowder for Pseudo-supercapacitors applications. Surfaces and Interfaces, 33, (2022) 102203. https://doi.org/10.1016/j.surfin.2022.102203

[19] E.T.D. Kumar, K. Thirumalai, S. Balachandran, R. Aravindhan, M. Swaminathan, J. Raghava Rao, Solar light driven degradation of post tanning water at heterostructured $BiVO_4$-ZnO mixed oxide catalyst interface. Surfaces and Interfaces, 8, (2017) 147–153. https://doi.org/10.1016/j.surfin.2017.05.009

[20] S. Muthamizh, J. Yesuraj, R. Jayavel, D. Contreras, K. Arul Varman, R.V. Mangalaraja, Microwave synthesis of β-$Cu_2V_2O_7$ nanorods: structural, electrochemical supercapacitance, and photocatalytic properties. Journal of Materials Science: Materials in Electronics, 32, (2021) 2744–2756. https://doi.org/10.1007/s10854-020-05007-w

[21] Z. Wang, W. Luo, S. Yan, J. Feng, Z. Zhao, Y. Zhu, Z. Li, Z. Zou, $BiVO_4$ nano–leaves: Mild synthesis and improved photocatalytic activity for O2 production under visible light irradiation. CrystEngComm, 13, (2011) 2500. https://doi.org/10.1039/C0CE00799D

[22] H.M. Zhang, J.B. Liu, H. Wang, W.X. Zhang, H. Yan, Rapid microwave-assisted synthesis of phase controlled $BiVO_4$ nanocrystals and research on photocatalytic properties under visible light irradiation. Journal of Nanoparticle Research, 10, (2008) 767–774. https://doi.org/10.1007/s11051-007-9310-y

[23] V.H. Nguyen, Q.T.P. Bui, D.-V.N. Vo, K.T. Lim, L.G. Bach, S.T. Do, T. Van Nguyen, V.D. Doan, T.D. Nguyen, T.D. Nguyen, Effective photocatalytic activity of sulfate-modified $BiVO_4$ for the decomposition of methylene blue under LED visible light. Materials, 12, (2019) 2681. https://doi.org/10.3390/ma12172681

[24] R. Gaur, P. Jeevanandam, Synthesis of SnS2 nanoparticles and their application as photocatalysts for the reduction of Cr(VI). Journal of Nanoscience and Nanotechnology, 18(1), (2018) 165–177. https://doi.org/10.1166/jnn.2018.14604

[25] H. Lin, H. Ye, S. Chen, Y. Chen, One-pot hydrothermal synthesis of BiPO4/$BiVO_4$ with enhanced visible-light photocatalytic activities for methylene blue degradation. RSC Advances, 4, (2014) 10968. https://doi.org/10.1039/C3RA45288C

[26] G.S. Kamble, Y.C. Ling, Solvothermal synthesis of facet-dependent $BiVO_4$ photocatalyst with enhanced visible-light-driven photocatalytic degradation of organic pollutant: assessment of toxicity by zebrafish embryo. Scientific Reports, 10, (2020). https://doi.org/10.1038/s41598-020-69706-4

[27] H. Cai, L. Cheng, F. Xu, H. Wang, W. Xu, F. Li, Fabrication of the heterojunction catalyst BiVO4 /P25 and its visible-light photocatalytic activities. Royal Society Open Science, 5, (2018) 180752. https://doi.org/10.1098/rsos.180752

[28] M.M. Sajid, N. Amin, N.A. Shad, S.B. khan, Y. Javed, Z. Zhang, Hydrothermal fabrication of monoclinic bismuth vanadate (m-BiVO4) nanoparticles for photocatalytic degradation of toxic organic dyes. Materials Science and Engineering: B, 242, (2019) 83–89. https://doi.org/10.1016/j.mseb.2019.03.012

[29] W.H. Saputera, A.F. Amri, R.R. Mukti, V. Suendo, H. Devianto, D. Sasongko, Photocatalytic degradation of palm oil mill effluent (POME) waste using BiVO4 based catalysts. Molecules, 26, (2021) 6225. https://doi.org/10.3390/molecules26206225

[30] V. Pandey, N. Singh, F.Z. Haque, Enhancement in structural and optical properties of boron doped ZnO nanostructures synthesized by simple aqueous solution growth technique. Journal of Advanced Physics, 6, (2017) 358–366.

[31] S.R.M. Thalluri, C. Martinez-Suarez, A. Virga, N. Russo, G. Saracco, Insights from crystal size and band gap on the catalytic activity of monoclinic BiVO4. International Journal of Chemical Engineering and Applications, 4(5), (2013) 305–309. https://doi.org/10.7763/IJCEA.2013.V4.315

[32] D. Arivukarasan, C.R. Dhas, R. Venkatesh, S.E.S. Monica, A.J. Josephine, K.C.M. Gnanamalar, B. Subramanian, Template-free and cost-effective nebulizer spray-coated BiVO4 nanostructured thin films for photocatalytic applications. Applied Physics A, 126, (2020) 1-13. https://doi.org/10.1007/s00339-019-3261-x

[33] A.J. Josephine, C. Ravi Dhas, R. Venkatesh, D. Arivukarasan, A. Jennifer Christy, S. Esther

Santhoshi Monica, S. Keerthana, Effect of pH on visible-light-driven photocatalytic degradation of facile synthesized bismuth vanadate nanoparticles. Materials Research Express, 7, (2020) 015036. https://doi.org/10.1088/2053-1591/ab653f

[34] A. Umar, R. Kumar, G. Kumar, H. Algarni, S.H. Kim, Effect of annealing temperature on the properties and photocatalytic efficiencies of ZnO nanoparticles. Journal of Alloys and Compounds, 648, (2015) 46–52. https://doi.org/10.1016/j.jallcom.2015.04.236

[35] M.A. Mahmoud, A. Poncheri, Y. Badr, M.G. Abd El Wahed, Photocatalytic degradation of methyl red dye. South African Journal of Science, 105(7), (2010). https://sajs.co.za/article/view/10291

[36] M. Guo, Q. He, A. Wang, W. Wang, Z. Fu, A novel, simple and green way to fabricate $BiVO_4$ with excellent photocatalytic activity and its methylene blue decomposition mechanism. Crystals, 6(7), (2016) 81. https://doi.org/10.3390/cryst6070081

[37] M. Kumar, R. Vaish, Photocatalytic dye degradation using $BiVO_4$–paint composite coatings. Materials Advances, 3, (2022) 5796–5806. https://doi.org/10.1039/D2MA00316C

[38] P. Amornpitoksuk, S. Suwanboon, S. Sangkanu, A. Sukhoom, N. Muensit, J. Baltrusaitis, Synthesis, characterization, photocatalytic and antibacterial activities of Ag-doped ZnO powders modified with a diblock copolymer. Powder Technology, 219, (2012) 158–164. https://doi.org/10.1016/j.powtec.2011.12.032

[39] P. Intaphong, A. Phuruangrat, P. Pookmanee, Synthesis and characterization of $BiVO_4$ photocatalyst by microwave method. Integrated Ferroelectrics, 175, (2016) 51–58. https://doi.org/10.1080/10584587.2016.1200910

[40] Z. Zhu, L. Zhang, J. Li, J. Du, Y. Zhang, J. Zhou, Synthesis and photocatalytic behavior of $BiVO_4$ with decahedral structure. Ceramics International, 39(7), (2013) 7461–7465. https://doi.org/10.1016/j.ceramint.2013.02.093

[41] R. Sharma, Uma, S. Singh, A. Verma, M. Khanuja, Visible light induced bactericidal and photocatalytic activity of hydrothermally synthesized $BiVO_4$ nano-octahedrals. Journal of Photochemistry and Photobiology B: Biology, 162, (2016) 266–272. https://doi.org/10.1016/j.jphotobiol.2016.06.035

Authors Contribution Statement

Rehna Parameswaran - Methodology, Investigation, Formal analysis, Data curation, Writing– original draft. Senthil Kumar Nagarajan- Conceptualization, Methodology, Validation, Supervision, Formal analysis, Writing original draft, Writing – review & editing. Chandrasekar Sivakumar- Formal analysis, Validation, Writing – review & editing. Balachandran Subramanian - Validation, Writing – review & editing. Raju S- Writing – review & editing, Mohanraj Kumar- Writing – review & editing. All the read and approved the final version of the manuscript.

Funding

The authors declare that no funds, grants or any other support were received during the preparation of this manuscript.

Competing Interests

The authors declare that there are no conflicts of interest regarding the publication of this manuscript.

Data Availability

The data supporting the findings of this study can be obtained from the corresponding author upon reasonable request.

Has this article screened for similarity?

Yes

About the License